Synchrotron X-ray computed laminography of the 3-D anatomy of tomato leaves

Pieter Verboven[1] Els Herremans[1], Lukas Helfen[2,4], Quang Tri Ho[1], Metadel Abera[1], Tilo Baumbach[2,4], Martine Wevers[3] and Bart M. Nicolaï[1]

[1] Division BIOSYST-MeBioS, Katholieke Universiteit Leuven, B-3001 Leuven, Belgium.
[2] IPS / ANKA, Karlsruhe Institute of Technology, PO Box 3640, 76021 Karlsruhe, Germany
[3] Research group of Materials Performance and Non-destructive Evaluation, Katholieke Universiteit Leuven, Kasteelpark Arenberg 44, BE-3001 Leuven, Belgium
[4] European Synchrotron Radiation Facility, 38043 Grenoble Cedex, France

One sentence summary: Synchrotron X-ray computed laminography allows the analysis of the anatomy of unprocessed leaves to quantify in 3-D the dimensions of cells and air spaces of mesophyll tissues and enables the generation of 3-D computer models of leaf segments.

Summary

Synchrotron radiation computed laminography (SR-CL) is presented as an imaging method to analyze the three-dimensional anatomy of leaves. SR-CL provided 3-D images of 1 mm² samples of intact leaves at a pixel resolution of 750 nm. The method allowed visualization and quantitative analysis of palisade and spongy mesophyll cells, and showed local venation patterns, aspects of xylem vascular structure and stomata. The method failed in imaging subcellular organelles such as chloroplasts. 3-D computer models of leaves were constructed that can provide a basis for calculating gas exchange, light penetration and water and solute transport. The leaf anatomy of two different tomato genotypes grown in saturating light conditions were compared by 3-D analysis. Differences were found in calculated values of tissue porosity, cell number density, cell area to volume ratio and cell volume and cell shape distributions of palisade and spongy cell layers. In contrast, mesophyll exposed cell area to leaf area ratio, a descriptor that correlates to maximum photosynthesis rate in saturated light conditions, was not different between spongy and palisade cells as well as between genotypes. Using 3-D image processing, many of the limitations of anatomical analysis with 2-D sections could be avoided.

OBJECTIVES

The aim of this work was to perform high-resolution laminography of leaf anatomy in order to verify if

(1) 3-D models of the leaf microstructure can be reconstructed that distinguish spongy and palisade mesophyll cells and their connectivity, the 3-D gas space network and the epidermis with stomata.

(2) 3-D image processing allows to calculate anatomical properties of leaves of two tomato (*Solanum esculentum* L.) genotypes.

Leaves were imaged by means of phase contrast SR-CL at the European Synchrotron Radiation Facility ESRF (Grenoble, France). Images were reconstructed in 3-D processed to quantitatively determine anatomical differences in leaves two tomato genotypes grown under identical conditions. The obtained 3-D leaf computer models will be the basis for the development of a 3-D model of photosynthesis that incorporates the microstructure of the leaf. Two cultivars were chosen based on their high commercial relevance but producing different types of tomato fruit: 'Growdena' is a common beef tomato cultivar, while 'Doloresse' is a genotype producing increasingly popular large cluster tomatoes. Both cultivars produce a dense vegetation and have medium productivity (Research Centre Hoogstraten, Belgium).

RESULTS

3-D leaf microstructure at submicron resolution

Figure 1 shows a sample leaflet in the synchrotron setup. SR-CL allowed a complete leaflet to be mounted on the rotation table. The leaflet was held into place between two

glass plates using agar strips at the edges of the plates that allow sealing the sample

holder without compressing the leaflet. The inclined rotation provided the same

visualization angle (with respect to the leaf's surface) for each projection image in such a

way that the penetration thickness in the leaflet remains approximately the same. Due to

only slowly varying X-ray transmission, this enabled high quality reconstructions of 3-D

images of the region of interest through the leaflet via a filtered-back projection algorithm

(Myagotin *et al*., 2013).

Figure 2 shows different lateral reconstructed cross sections of a tomato leaflet though the

different tissues, namely the adaxial epidermis, palisade mesophyll, spongy mesophyll

with vascular bundles and the abaxial epidermis. Also a transverse section is given

through the different tissues. The phase contrast at the air-cell interphases was evidenced

by darker and brighter pixels marking the transition from air to cell (Figure 2E). The

contrast difference between cells and intercellular spaces themselves was small, thus only

the phase contrast could be used to distinguish the two zones. The irregular cell shapes of

the tightly packed epidermis cells can be distinguished in Figure 2A and 2D. The circular

cross sections of the palisade cells appeared rather uniform in diameter (Figure 2B),

while the spongy mesophyll consisted of clusters of more irregular cells of different sizes

(Figure 2C). In Figure 2C, a secondary vein with two smaller veins emerging from it can

be distinguished.

Figure 3 presents lateral cross sections that contain several microstructural details of the

different tissues. The epidermis is a very dense layer of single cells without air spaces

between them. At the surface the epidermis cells could be recognized from their puzzle-

piece shape (Figure 3A), but the outline between the cells within the epidermis layer was

not discerned (Figure 2E). Therefore, it was impossible to identify accurately individual epidermis cells in the images. The guard cells were were visible by their kidney shape, attached to each other by their two ends of the concave sides, and forming a central pore. The slim stomatal pore was visible as a slit in the X-ray SR-CL images and the contours of the guard cells could be distinguished from the epidermis, giving an indication of where they are and of their approximate size (Figure 3A). In Figure 3A, stomata are seen for the abaxial side of the leaves. The adaxial epidermis did not contain any stomata in the imaged leaves.

Figure 3B shows details of a secondary vascular bundle, where the trachedial elements of the xylem are highlighted as a result of the phase contrast. The surrounding cells of the xylem bundles were not clearly separated. It was thus impossible to identify where phloem tissue and supporting collenchyma are and what their cell structure is. Figure 3C shows three interconnected vascular bundles, where the central xylem vessel is contrasted and completed surround by supporting cells of the bundles. From the bundles the connections to the spongy cells could be seen forming a network through the mesophyll. In Figure 3C a particular cell type is contrasted from the others. These were presumably cells with more abundantly present starch-containing plastids that were picked up by the phase contrast (Cloetens *et al*., 2006), and they are distributed across the entire spongy mesophyll. However, the number of such cells in the image appears small which could be indicative of fully expanded leaves.

3-D leaf structure models

The stacks of reconstructed lateral cross sections were combined to obtain a 3-D microstructure image of the leaves. The individual cell volumes of the palisade and spongy mesophyll were segmented from the intercellular air space. As the phase contrast between touching cells was insufficient, semi-manual cell segmentation was performed using the wrapping tool of Avizo after marking individual cell cross-sectional areas on three perpendicular planes. As a result, 3-D models of leaves of 'Doloresse' and 'Growdena' genotypes were obtained, in which individual cell volumes are labeled. Figures 4A and B present 3-D models of three samples of 'Doloresse' and 'Growdena' leaves, respectively. Only on the abaxial side, stomata were segmented (colored in blue). In the bottom image of Figure 4A a part of a trichome on the abaxial side is seen. The 3-D models confirmed the expected shapes seen on the cross sections, cylindrical palisade cells and small irregular spongy cells, and provided a means to compare different genotypes.

Figure 5 plots the obtained 3-D network of air spaces inside the leaf using a skeleton analysis. In both cultivars it was seen that larger substomatal cavities in the spongy mesophyll and narrow air channels in the palisade form a continuous network. In Figure 5 the good connectivity of the air spaces inside the leaf is visualised, while connectivity to the external air is limited to the stomata in the abaxial side of the leaves. The adaxial surface topography of the leaf in Fig. 6B is characterized by more pronounced microscopic valleys in between neighbouring, more concave, cell surfaces but these dips in the surface are not connected to the internal air space of the leaf. The 3-D structure of the leaves was further analyzed quantitatively below, but can also be the geometrical

input for more advanced photosynthesis models by introducing the real leaf microstructure into a computational framework.

Quantitative analysis of leaf microstructure

The 3-D models obtained from SR-CL were analyzed in terms of volume and shape characteristics. The results are presented in Figures 6 and 7 and Table 1. The leaves of 'Doloresse' and 'Growdena' were significantly different in some of these parameters. The thickness of 'Growdena' (196 ± 29 µm) leaves was on average almost 40 µm higher than that of 'Doloresse' (158 ± 9 µm) . All tissues were thicker, and the main differences are found in the palisade and spongy layers (Table 1). The number of cells per unit area tended to vary considerably from one leaf to another, indicative of considerable variations in leaf structures. The 'Doloresse' samples had a higher average number of palisade and spongy cells than 'Growdena', but this difference was only just significant for palisade cells (Table 1).

Figure 6 shows the distribution of cell volumes for the two genotypes and for palisade and spongy mesophyll, separately. While the palisade mesophyll had a normal cell volume distribution, spongy tissue was characterized by a skewed distribution with a small but significant contribution of larger cells (skewness of the distribution > 2). Major differences between 'Growdena' and 'Doloresse' were found. Spongy tissue in the two cultivars was characterized by similar cell volume distributions, although a significant difference ($p < 0.05$) exists in particular for the proportion of small spongy cells: The proportion of cells smaller than 3000 µm³ was significantly larger for 'Growdena' (Figure 6). The palisade was distinctly different between the two genotypes. The 'Growdena'

samples possessed palisade cells that are on average more than 2 times larger in volume than 'Doloresse'. These data are indicative of the fact that in 'Growdena', the palisade cells are larger in both length and diameter.

Figure 7 presents the sphericity distribution of the cells. Sphericity was expressed as the ratio of the surface area of a sphere with the same volume of the cell to the actual surface area of the cell. For a perfectly round shape, the value of sphericity is 1, deformed shapes have significantly smaller values. The sphericity of cells followed a normal distribution (Figure 7). No relationship between sphericity and cell volume was found. A large range of shapes was evident for the spongy cells (Figure 7B) with the sphericity ranging from 0.4 to 1. The palisade cells were mainly contained within a narrow band of sphericity values of 0.6 to 0.8 (Figure 7A). The sphericity thus expressed the more uniform shape distribution of the palisade cells. The sphericity of a perfect cylinder is 0.874; the lower values here were due to the imperfect shapes of the cells with curved surfaces and unequal diameters along the major axis of the cells. While differences in shape between spongy and palisade cells have been known for a long time, here we were able to measure the variation of this parameter from actual 3-D images of the cells.

With respect to the gas exchange, the volume of intercellular air spaces and cell surface characteristics are important (Table 1). The two genotypes possessed a very similar porosity, which is on average 0.41 ± 0.05 and 0.40 ± 0.04, respectively for 'Doloresse' and 'Growdena'. The porosity of the two mesophyll layers does differ for each cultivar, with higher porosity for the spongy than for the palisade mesophyll (Table 1). Also, one could imagine using number density, average cell volume and layer thickness to calculate a rough estimate of porosity of each layer in each genotype. Using the average values in

Table 1, we find the following porosity estimates for palisade and spongy mesophyll of 52% and 72%, and 32% and 74%, , respectively for Doloresse and Growdena. Although numerically different from the values obtained from the images, the estimates confirm the differences between the values between mesophyll layers. Taking the relative contributions of each layer into the total leaf thickness into account, the total porosity estimate of the two genotypes is 48 and 47%, thus also confirming the negligible differences given in Table 1.

The pore structure was also represented as a network of interconnected tubes with radii representing the local pore size (Figure 5). Individual pores of the network had radii in the range of 1.5 to 50 µm in both cultivars. With the smaller pores in the palisade, the porosity in this tissue was also about half of that of the spongy mesophyll layer (Table 1). The surface of the cells exposed to the intercellular spaces was calculated to assess the available exposed cell area to gas exchange. The resulting cell area to cell volume ratio was similar between the two tomato genotypes. On average, these ratios were higher for the smaller and more spherical spongy cells (Table 1). Finally, the cell surface area to leaf surface area ratio expresses the increase in gas exchange surface that is created by the porous tissue structure of the leaves. The average values for this ratio were higher than 6, meaning that the exposed cell area for gas exchange in leaves was at least six times higher than the one-sided leaf surface area. For both palisade and spongy tissue, 'Doloresse' had on average smaller ratios than 'Growdena', but the differences were not significant. Further, the more densely packed palisade cells still had a similar exchange surface ratio compared to the spongy cells (Table 1).

Finally, the distribution of stomata varied considerably between samples leading to insignificant differences between the two genotypes (Table 1).

CONCLUSIONS

Synchrotron radiation X-ray computed laminography was successful in obtaining 3-D computer models of leaf anatomy from intact leaves. Today the technique has limited availability to the plant science community as it is only available at the synchrotron facility. However, X-ray computed laminography, if made possible on more widely available laboratory scale CT devices, could provide a useful technique for 3-D imaging of leaf tissues, overcoming some of the limitations of tomography and laser scanning techniques. The technique does generate large datafiles, which are inherent to 3-D datasets, which require dedicated image processing, which is becoming more widespread available with commercial visualization and analysis software.

The measured spatial distribution of stomata in direct connection with the internal gas space network and mesophyll morphology will allow integral analysis of leaf anatomy on plant hydraulics, gas and metabolites transport using computational approaches. With the development of computer models it is expected that rapid progress can now be made in the assessment of the functional importance of anatomic properties of leaf tissues, rather than just comparing anatomical differences between geno- and phenotypes.

PUBLICATIONS OUTPUT
Synchrotron X-ray computed laminography of the three-dimensional anatomy of tomato leaves. Verboven et al. (2014) the Plant Journal 81, 169.

http://onlinelibrary.wiley.com/doi/10.1111/tpj.12701/full

3-D microscale modeling of CO2 transport and light propagation in tomato leaves

enlightens photosynthesis. Ho et al. (2015) Plant, Cell & Environment (accepted). DOI:

10.1111/pce.12590

Modeling the propagation of light in realistic tissue structures with MMC-fpf: a meshed

Monte Carlo method with free phase function. Watté et al. (2015) Optics Express 23,

17467. doi: 10.1364/OE.23.017467.

MATERIALS AND METHODS

Materials

Young tomato plants (*Solanum lycopersicum* L.) of the cultivars 'Growdena' and

'Doloresse' were obtained from BPK (Belgische Planten Kwekerij, Duffel, BE) on

16/02/2010. 'Growdena' is a beef tomato cultivar, 'Doloresse' produces large cluster

tomatoes. Both cultivars have a dense vegetation and medium productivity (Research

Centre Hoogstraten, Belgium). Plants were grown for 12 days in controlled conditions in

a greenhouse at KU Leuven (BE) until transport to the experimental facility at European

Synchrotron Radiation Facility ESRF (FR). A dedicated nutrient solution was applied to

the plants containing KNO_3, $Ca(NO_3)_2$, Fe-EDTA, $MgSO_4$, KH_2PO_4, K_2SO_4, $MnSO_4$,

$CuSO_4$, $ZnSO_4$, $Na_2B_4O_7$ and Na_2MoB_4. The solution EC was 2.62 mS/cm and the pH

was equal to 5.52. Plants were placed in a rockwool substrate and irrigated with the

nutrient solution. The environmental conditions were 18.8 ± 2.2 °C and 70.5 ± 3.2 %RH,

the average day-time PAR was 328 μmol m^{-2} s^{-1} and the maximum daily PAR was $1112 \pm$

543 μmol m^{-2} s^{-1} (standard deviations given). Plants were taken by car to ESRF and kept

at room temperature close to the window near the experimental room of beamline ID19 of ESRF for the duration of the experiment (3 days), with daily irrigation. Earlier examination of the surface of adaxial and abaxial sides of leaves of Growdena with SEM (not shown) revealed that tomato leaves are essentially hypostomatous: stomata were more abundantly present on the abaxial side than on the adaxial side. At the time of the experiments the plants were still in the vegetative growth stage and were approximately 1 m high.

We selected the distal-side leaflets from the fourth leaf below the top-most fully grown leaf for measurements. One leaf from each of three plants per cultivar was used. Leaflet samples were taken from the lower compound leaves directly before each SR-CL experiment. The petiolule and thicker parts of the central nerve were removed from the leaflet. The leaflet was then placed between two square glass plates of 2 mm thick and dimensions of 158 by 158 mm, which fit the laminography sample holder at ESRF. In order not to compress and damage the sample between the glass plates when the glass plates were attached on the sample holder, dots of agar solution were distributed around the sample before putting the top plate.

Synchrotron X-ray laminography

The experiments were conducted on the laminography set-up installed by the Karlsruhe Institute of Technology (KIT, Karlsruhe, Germany) at beamline ID19 of the European Synchrotron Radiation Facility (ESRF, Grenoble, France). This is a long (150 m) imaging beamline (Weitkamp *et al*., 2010) where the spatial coherence of the beam is particularly large (transverse coherence length in the order of 100 μm), which allows phase-contrast

imaging where the phase of the X-ray beam transmitted by the sample is shifted due to the interaction with the electrons in the material. Imaging using phase contrast, as opposed to absorption contrast, is a powerful method for the investigation of light materials, but also to distinguish, in absorbing materials, phases with very similar X-ray attenuation but different electron densities (Cloetens *et al*., 2006). In this study, it is efficiently used for edge detection at cell-cell interfaces where absorption images have insufficient contrast.

The X-ray beam generated from a variable-gap undulator with 32 mm magnetic-field period was monochromatized to 18 keV using an artificial multilayer monochromator. The selected 2D detector was based on a FReLoN camera (Labiche et al., 2007); a CCD camera with a 2048 x 2048 pixel chip and 14 bit dynamic range. The CCD was optically coupled to an X-ray/visible light converter screen using a microscope system (Douissard *et al*., 2012) with effective 20x magnification, providing a field of view of 1.54×1.54 mm^2 and, without binning, an image pixel size of 750 nm. The pixel size of the images was calculated optically. To verify it we move a precise motor step-wise by a (small) known amount (e.g. by a tenth of the field of view) and fit the distances to the known displacements. The spatial resolution realised in these experiments is largely determined by the detector performance. It has actually not been determined during this measurement campaign but the detectors are regularly checked to provide a true spatial resolution in the order of 2 to 3 pixels (corresponding to 2 to 3 voxels in-plane resolution). The mechanical performance of the instrument has been shown not to have a significant impact on the resolution at the pixel sizes employed.

To minimize radiation dose to the specimen a fast X-ray shutter was installed. A total of 1200 projections with an exposure time of 0.5 s was acquired for each sample during a continuous rotation over 360 degrees. Scan time was maximally 10 minutes per sample. The incident X-ray flux was reduced below the threshold for unrecoverable specimen damage. A sample-detector distance of 35 mm was chosen to operate in phase contrast mode. The laminographic reconstruction was performed with a software developed in-house employing a filtered-back projection algorithm (Myagotin *et al.,* 2013), after correction for sample motion using the GNU Octave software (http://www.gnu.org/software/octave/). Volume renderings and quantitative measurements on the sample were obtained by 3-D image segmentation and isosurface representations with Avizo Fire (Visualization Group Sciences, Merignac, FR). For each sample a zone of $250 \times 250 \times 500$ voxels was analysed. Quantitative analysis was performed by means of calculating the volume and surface area of the labelled cells in the tissues after manual segmentation using the wrapping tool in Avizo. Statistics on probability functions were performed in Matlab (The Mathworks, Natick, MA) using the Kolmogorov-Smirnov test. Air spaces were segmented from cells by means of manual thresholding of the images. Porosity was calculated as the proportion of the total air space volume over total leaf volume of each sample.

Acknowledgements

LITERATURE

Aalto, T. and Juurola, E. (2002) A three-dimensional model of CO_2 transport in airspaces and mesophyll cells of a silver birch leaf. *Plant Cell Environ.,* **25**, 1399-1409.

Altapova, V., Helfen, L., Myagotin, A., Hanschke, D., Moosmann, J., Gunneweg, J. and Baumbach, T. (2012) Phase contrast laminography based on Talbot interferometry. *Optics Express,* **20**, 6496-6508.

Armstrong, J., Jones, R.E. and Armstrong, W. (2006) Rhizome phyllosphere oxygenation in *Phragmites* and other species in relation to redox potential, convective gas flow, submergence and aeration pathways. *New Phytol.,* **172**, 719-731.

Barbour, M.M., Warren, C.R., Farquhar, G.D., Forrester, G. and Brown, H. (2010) Variability in mesophyll conductance between barley genotypes, and effects on transpiration efficiency and carbon isotope discrimination. *Plant Cell Environ.,* **33**, 1176-1185.

Bernacchi, C.J., Bagley, J.E., Serbin, S.P., Ruiz-Vera, U.M., Rosenthal, D.M. and Vanloocke, A. (2013) Modelling C_3 photosynthesis from the chloroplast to the ecosystem. *Plant Cell Environ.,* doi: 10.1111/pce.12118.

Betz ,O., Wegst, U., Weide, D., Heethoff, M., Helfen, L., Lee, W.K. and Cloetens, P. (2007) Imaging applications of synchrotron X-ray phase-contrast microtomography in biological morphology and biomaterials science. 1. General aspects of the technique and its advantages in the analysis of millimetre-sized arthropod structure. *J Micro.,* **227**, 51-71.

Blonder, B., De Carlo, F., Moore, J., Rivers, M. and Enquist, B.J. (2012) X-ray imaging of leaf venation networks. *New Phytol.,* **196**, 1274-1282.

Bongi, G. and Loreto, F. (1989) Gas-exchange properties of salted-stressed olive (*Olea europea* L.) leaves. *Plant Physiol.,* **90**, 1408-1416.

Brodersen, C.R. and Vogelmann, T.C. (2010) Do changes in light direction affect absorption profiles in leaves? *Functional Plant Biol.,* **37**, 403-412.

Busch, F.A., Sage, T.L., Cousins, A.B. and Sage, R.F. (2013) C_3 plants enhance rates of photosynthesis by reassimilating photorespired and respired CO_2. *Plant Cell Environ.,* **36**, 200-212.

Cloetens, P., Pateyron-Salomé, M., Buffière, J.Y., Peix, G., Baruchel, J., Peyrin, F., Schlenker, M. (1997) Observation of microstructure and damage in materials by phase sensitive radiography and tomography. *J Appl Phys.,* **81**, 5878-5886.

Cloetens, P., Mache, R., Schlenker, M. and Lerbs-Mache, S. (2006) Quantitative phase tomography of *Arabidopsis* seeds reveals intercellular void network. *Proc Natl Acad Sci., USA,* **103**, 14626–14630.

Colmer, T.D. and Pederson, O. (2008) Underwater photosynthesis and respiration in leaves of submerged wetland plants: gas films improve CO_2 and O_2 exchange. *New Phytol.,* **177**, 918-926.

Defraeye, T., Verboven, P., Derome, D., Carmeliet, J and Nicolai, B. (2013a) Stomatal transpiration and droplet evaporation on leaf surfaces by a microscale modelling approach. *Int J Heat Mass Transfer,* **65**, 180-191.

Defraeye, T., Verboven, P., Ho, Q. and Nicolai, B. (2013b) Convective heat and mass exchange predictions at leaf surfaces: applications, methods and perspectives. *Comp Electr Agricul.,* **96**, 180-201.

Defraeye, T., Aregawi, W., Cantré, D., Hartmann, S., Lehmann, E., Carmeliet, J., Verboven, P., Derome, D. and Nicolai, B. (2013c) Quantitative neutron imaging of water distribution, venation network and sap flow in leaves. In preparation.

Dhondt, S., Vanhaeren, H., Van Loo, D., Cnudde, V. and Inzé, D. (2010) Plant structure visualization by high-resolution X-ray computed tomography. *Trends Plant Sci.,* **15**, 419-422.

Di Marco, G., Manes, F., Tricoli, D. and Vitale, E. (1990) Fluorescence parameters measured concurrently with net photosynthesis to investigate chloroplastic CO_2 concentration in leaves of Quercus ilex L. *J Plant Physiol.,* **136**, 538-543.

Dobbins, J.T. and Godfrey, D.J. (2003) Digital X-ray tomosynthesis: current state of the art and clinical potential. *Phys Med Biol.,* **48**, R65-R106.

Dorca-Fornell, C., Pajor, R., Lehmeier, C., Pérez-Bueno, M., Bauch, M., Sloan, J., Osborne, C., Rolfe, S., Sturrock, C., Mooney, S. and Fleming, A. (2013). Increased leaf mesophyll porosity following transient retinoblastoma-related protein

silencing is revealed by microcomputed tomography imaging and leads to a system-level physiological response to the altered cell division pattern. *Plant J.,* **76**, 659-640.

Douissard, P-A., Cecilia, A., Rochet, X., Chapel, X., Martin, T., van de Kamp, T., Helfen, L., Baumbach, T., Luquot, L., Xiao, X., Meinhardt, J. and Rack, A. (2012) A versatile indirect detector design for hard X-ray microimaging, *J. Instrumentation,* **7**, P09016

Evans, J.R., von Caemmerer, S., Setchell, B.A., Hudson, G.S. (1994) The relationship between CO_2 transfer conductance and leaf anatomy in transgenic tobacco with a reduced content of Rubisco. *Aust. J. Plant Phys.*, **21**, 475-495

Evans, J.R. and von Caemmerer, S. (1996) Carbon dioxide diffusion inside leaves. *Plant Physiol.,* **110**, 339-346.

Evans, J.R. (1999) Leaf anatomy enables more equal access to light and CO_2 between chloroplasts. *New Phytol.,* **143**, 93-104.

Evans, J.R. and Vogelmann, T.C. (2003) Profiles of ^{14}C fixation through spinach leaves in relation to light absorption and photosynthetic capacity. *Plant Cell Environ.,* **26**, 547-560.

Evans, J.R. (2009) Potential errors in electron transport rates calculated from chlorophyll fluorescence as revealed by a multilayer leaf model. *Plant and Cell Physiol.,* **50**, 698-706.

Evans, J.R., Kaldenhoff, R., Genty, B. and Terashima, I. (2009) Resistances along the CO_2 diffusion pathway inside leaves. *J Exp Bot.,* **60**, 2235–2248.

Evans, J.R., von Caemmerer, S. (2011) Enhancing Photosynthesis. *Plant Physiol.,* **155**, 19.

Flexas, J., Diaz-Espejo, A., Galmés, J., Kaldenhoff, R., Medrano, H. et al. (2007) Rapid variation of mesophyll conductance in response to changes in CO_2 concentration around leaves. *Plant Cell Environ.,* **30**,1284-1298.

Flexas, J., Ribas-Carbó, M., Diaz-Espejo, A., Galmés, J. and Medrano, H. (2008) Mesophyll conductance to CO_2: current knowledge and future prospects. *Plant Cell Environ.,* **31**, 602-621.

Flexas, J., Barbour, M.M., Cabrera, H.M. et al. (2012) Mesophyll diffusion conductance to CO2: an unappreciated central player in photosynthesis. *Plant Sci.,* **193-194**, 70-84.

Galmés, J., Ochogaviá, J.M., Gago, J., Roldán, E.J., Cifre, J., Conesa, M.A. (2013). Leaf responses to drought stress in Mediterranean accessions of *Solanum lycopersicum*: anatomical adaptations in relation to gas exchange parameters. *Plant Cell Environ.*, **36**, 920-935.

Griffiths, H. and Helliker, B.R. (2013) Mesophyll conductance: internal insights of leaf carbon exchange. *Plant Cell Environ.,* **36**, 733–735.

Harasse, S., Hirayama, N., Yashiro, W. and Momose, A. (2010) X-ray Phase laminography with talbot interferometer. *Developments in X-ray tomography* VII **7804**, 780411.

Harasse, S., Yashiro, W. and Momose, A. (2012) X-ray phase laminography with a grating interferometer using iterative reconstruction. *AIP Conf Proc.,* **1466**, 163. doi: 10.1063/1.4742286.

Harley, P.C., Loreto, F., Di Marco, G. and Sharkey, T.D. (1992) Theoretical considerations when estimating the mesophyll conductance to CO_2 flux by analysis of the response of photosynthesis to CO_2. *Plant Physiol.,* **98**, 1429-1436.

Hassiotou, F., Evans, J.R., Ludwig, M. and Veneklaas, E.J. (2009). Stomatal crypts may facilitate diffusion of CO2 to adaxial mesophyll cells in thick sclerophylls. *Plant Cell Environ.* **32**, 1596-1611.

Helfen, L., Baumbach, T., Mikulík, P., Kiel, D., Pernot, P., Cloetens, P. and Baruchel, J. (2005) High-resolution three-dimensional imaging of flat objects by synchrotron-radiation computed laminography. *Appl Phys Lett.,* **86**, 071915.

Helfen, L., Myagotin, A., Pernot, P., Di Michiel, M., Mikulík, P., Berthold, A. and Baumbach, T. (2006) Investigation of hybrid pixel detector arrays by synchrotron-radiation imaging. *Nuclear Instruments and Methods in Physics Research Section A: Accelerators, Spectrometers, Detectors and Associated Equipment,* **563**, 163-166.

Helfen, L., Myagotin, A., Rack, A., Pernot, P., Mikulík, P., Di Michiel, M. and Baumbach, T. (2007) Synchrotron-radiation computed laminography for high-resolution three-dimensional imaging of flat devices. *Phys Stat Sol. (a),* **204**, 2760–2765.

Helfen, L., Baumbach, T., Cloetens, P. and Baruchel, J. (2009) Phase-contrast and holographic computed laminography. *Appl Phys Lett.,* **94**, 104103.

Helfen, L., Myagotin, A., Mikulík, P., Pernot, P., Voropaev, A., Elyyan, M., Di Michiel, M., Baruchel, J. and Baumbach, T. (2011) On the implementation of computed laminography using synchrotron radiation. *Rev Sci Instruments,* **82**, 063702.

Ho, Q., Verboven, P., Verlinden, B., Herremans, E., Wevers, M., Carmeliet, J. and Nicolai, B. (2011) A 3-D multiscale model for gas exchange in fruit. *Plant Physiol.,* **155**, 1158-1168.

Ho, Q.T., Verboven, P., Yin, X., Struik, P.C. and Nicolaï, B.M. (2012) A microscale model for combined CO_2 diffusion and photosynthesis in leaves. *PloS One,* **7**, e4837.

Karahara, I., Umemura, K., Soga, Y., Akai, Y., Bando, T., Ito, Y., Tamaoki, D., Uesugi, D., Abe, J., Yamauchi, D. and Mineyuki, Y. (2012) Demonstration of osmotically dependent promotion of aerenchyma formation at different levels in the primary roots of rice using a 'sandwich' method and X-ray computed tomography. *Ann Bot.,* **110**, 503-9.

Krug, K., Porra, L., Coan, P., Tauber, G., Wallert, A., Dik, J., Coerdt, A., Bravin, A., Elyyan, M., Helfen, L. and Baumbach, T. (2008) Relics in Medieval Altarpieces? Combining X-ray tomographic, laminographic and Phase-Contrast Imaging to Visualize Thin Organic Objects in Paintings. *J Synchr Rad.,* **15**, 55-61.

Labiche, J-C., Mathon, O., Pascarelli, S., Newton, M.A., Guilera Ferre, G., Curfs, C., Vaughan, G. and Homs, A. (2007) The fast readout low noise camera as a versatile X-ray detector for time resolved dispersive extended X-ray absorption fine structure and diffraction studies of dynamic problems in materials science, chemistry, and catalysis. *Sci Instruments,* **78**, 091301.

Leroux, O., Leroux, F., Bellefroid, E., Claeys, M., Couvreur, M., Borgogne, G., Van Hoorebeke, L., Masschaele, B. and Viane, R. (2009) A new preparation method to

study fresh plant structures with X-ray computed tomography. *J Microscopy,* **233**, 1-4.

Maricle, B.R., Koteyeva, N.K., Voznesenskaya, E.V., Thomasson, J.R. and Edwards, G.E. (2009) Diversity in leaf anatomy, and stomatal distribution and conductance, between salt marsh and freshwater species in the C4 genus *Spartina* (Poaceae). *New Phytol*., **184**, 216–233.

Mayo, S.C. and Evans, R. (2010) Micron-scale 3-D imaging of wood and plant microstructure using high-resolution X-ray phase-contrast microtomography. *J Struc Biol.,* **171**, 182-188.

Mendoza, F., Verboven, P., Mebatsion, H.K., Kerckhofs, G., Wevers, M. and Nicolai, B. (2007) Three-dimensional pore space quantification of apple tissue using X-ray computed microtomography. *Planta,* **226**, 559-570.

Moffat, A.J., Wright, P., Helfen, L., Baumbach, T., Johnson, G., Spearing, S.M. and Sinclair, I. (2010) In situ synchrotron computed laminography of damage in carbon fibre – epoxy [90/0]s laminates. *Scripta Mater.,* **62**, 97-100.

Morgeneyer, T.F., Helfen, L., Sinclair, I., Proudhon, H., Xu, F. and Baumbach, T. (2011) In situ observation of ductile crack initiation and propagation in an Al alloy via synchrotron radiation computed laminography. *Scripta Mater.* **65**, 1010–1013.

Myagotin, A., Voropaev, A., Helfen, L., Hänschke, D. and Baumbach, T. (2013) Efficient volume reconstruction for parallel-beam computed laminography by filtered backprojection on multi-core clusters. *IEEE Trans. Image Proc.* **22**, 5348-5361 .

Oguchi, R., Hikosaka, K. and Hirose, T. (2005) Leaf anatomy as a constraint for photosynthetic acclimation: differential responses in leaf anatomy to increasing growth irradiance among three deciduous trees. *Plant Cell Environ.* **28**, 916-927.

Palmer, D.A. and Bender, C.L. (1995) Ultrastructure of tomato leaf tissue treated with the pseudomonad phytotoxin coronatine and comparison with methyl jasmonate. *MPMI*, **8**, 683-693.

Parkhurst, D.F. (1994) Diffusion of CO_2 and other gases inside leaves. *New Phytol.,* **126**, 449–479.

Reischig, P., Helfen, L., Wallert, A., Baumbach, T. and Dik, J. (2013) Non-invasive, three-dimensional X-ray imaging of paint layers. *Appl Phys. A,* **111**, 983-995

Rezvani Moghaddam, P. and Wilman, D. (1998) Cell wall thickness and cell dimensions in plant parts of eight forage species. *J Agric Sci.,* **131**, 59–67.

Sage, T.L. and Sage, R.F. (2009) The functional anatomy of rice leaves: Implications for refixation of photorespiratory CO_2 and efforts to engineer C_4 photosynthesis into rice. *Plant Cell Physiol.,* **50**, 756–772.

Scippa, G.S., Di Michele, M., Onelli, E., Patrignani, G., Chiatante, D. and Bray, E.A. (2004) The histone-like protein H1-S and the response of tomato leaves to water deficit. *J Exp Bot.,* **55**, 99-109.

Sorrell, B.K. and Hawes, I. (2010) Convective gas flow development and the maximum depths achieved by helophyte vegetation in lakes. *Ann Bot.,* **105**, 165–174.

Sperry, J.S. (2000) Hydraulic constraints on plant gas exchange. *Agricul Forest Meterol.,* **104**, 13-23.

Stuppy, W.H., Maisano, J.A., Colbert, M.W., Rudall, P.J. and Rowe, T.B. (2003) Three-dimensional analysis of plant structure using high-resolution X-ray computed tomography. *Trends Plant Sci.,* **8**, 2-6.

Tazoe, Y., von Caemmerer, S., Estavillo, G.M. and Evans, J.R. (2011) Using tunable diode laser spectroscopy to measure carbon isotope discrimination and mesophyll conductance to CO_2 diffusion dynamically at different CO2 concentrations. *Plant Cell Environ.,* **34**, 580–591.

Terashima, I., Hanba, Y.T., Tholen, D. and Niinemets, U. (2011) Leaf functional anatomy in relation to photosynthesis. *Plant Physiol.,* **155**, 108-116.

Thain ,J.F. (1983). Curvature correction factors in the measurement of cell surface areas in plant tissues. *J. Exp. Bot*., **34**, 87-94.

Tholen, D., Boom, C., Noguchi, K., Ueda, S., Katase, T. and Terashima, I. (2008) The chloroplast avoidance response decreases internal conductance to CO_2 diffusion in *Arabidopsis thaliana* leaves. *Plant Cell Environ.,* **31**, 1688–1700.

Tholen, D. and Zhu, X-G. (2011) The mechanistic basis of internal conductance: a theoretical analysis of mesophyll cell photosynthesis and CO_2 diffusion. *Plant Physiol.,* **156**, 90–105.

Tholen, D., Ethier, G., Genty, B., Pepin, S. and Zhu, X.G. (2012) Variable mesophyll conductance revisited. Theoretical background and experimental implications. *Plant Cell Environ.,* **35**, 2087–2103.

Tomás, M., Flexas, J., Copolovici, L., Galmés, J., Hallik, L., Medrano, H., Ribas-Carbó, M., Tosens, T., Vislap, V. and Niinemets, Ü. (2013) Importance of leaf

anatomy in determining mesophyll diffusion conductance to CO_2 across species: quantitative limitations and scaling up by models. *J Exp Bo.*, doi:10.1093/jxb/ert086.

Ustin, S.L., Jacquemoud, S. and Govaerts. Y. (2001) Simulation of photon transport in a three-dimensional leaf: implications for photosynthesis. *Plant Cell Environ.* **24**, 1095-1103.

Verboven, P., Kerckhofs, G., Mebatsion, H.K., Ho, Q.T., Temst, K., Wevers, M., Cloetens, P. and Nicolaï, B.M. (2008) 3-D gas exchange pathways in pome fruit characterised by synchrotron X-ray computed tomography. *Plant Physiol.,* **147**,518-527.

Verboven, P., Pedersen, O., Herremans, E., Ho, Q.T., Nicolaï, B.M., Colmer, T.D. and Teakle, N. (2012) Root aeration via aerenchymatous phellem – 3-D micro-imaging and radial O_2 profiles in *Melilotus siculus*. *New Phytol.,* **193**, 420-431.

Verboven, P., Herremans, E., Borisjuk, L., Helfen, L., Ho, Q.T., Tschiersch, H., Fuchs, J., Nicolaï, B.M. and Rolletschek, H. (2013) Void space inside the developing seed of *Brassica napus* and the modelling of its function. *New Phytol.*, **199**, 936-947.

Vesala, T., Ahonen, T., Hari, P., Krissinel, E. and Shokhirev, N. (1996) Analysis of stomatal CO_2 uptake by a three-dimensional cylindrically symmetric model. *New Phytol.*, **132**, 235-245.

Vogelmann, T.C., Bornman, J.F. and Yates, D. (1996) Focusing of light by leaf epidermal cells. *Physiologia Plantarum,* **98**, 43–56.

Warren, C.R. (2008). Soil water deficits decrease the internal conductance to CO2 transfer but atmospheric water deficits do not. *J Exp Bot.,* **59**, 327-334.

Weitkamp, T., Tafforeau, P., Boller, E., Cloetens, P., Valade, J-P., Bernard, P., Peyrin, F., Ludwig, W., Helfen, L. and Baruchel, J. (2010) Parallel-beam imaging at the ESRF beamline ID19: current status and plans for the future. *AIP Conference Proceedings* 1234: 83-86

Wuyts, N., Palauqui, J.C., Conejero, G., Verdeil, J.L., Granier, C. and Massonnet, C. (2010) High-contrast three-dimensional imaging of the *Arabidopsis* leaf enables the analysis of cell dimensions in the epidermis and mesophyll. *Plant Methods,* **6**, 17-30.

Wuyts, N., Massonnet, C., Dauzet, M. and Granier, C. (2012) Structural assessment of the impact of environmental constraints on *Arabidopsis thaliana* leaf growth: a 3-D approach. *Plant Cell Environ.,* **35**, 1631-1646.

Xu, F., Helfen, L., Moffat, A.J., Johnson, G., Sinclair, I. and Baumbach, T. (2010) Synchrotron radiation computed laminography for polymer composite failure studies. *J Synchrotron Radiation,* **17**, 222-226.

Xu, F., Helfen, L., Baumbach, T. and Suhonen, H. (2012a) Comparison of image quality in computed laminography and tomography. *Optics Express,* **20**, 794-806.

Xu, F., Helfen, L., Suhonen, H., Elgrabli, D., Bayat, S., Reischig, P., Baumbach, T. and Cloetens, P. (2012b) Correlative Nanoscale 3-D Imaging of Electron Density and Elemental Composition in Extended Objects. *PloS ONE,* **7**, e50124.

Xu, C.Y., Salih, A., Ghannoum, O. and Tissue, D.T. (2012c). Leaf structural characteristics are less important than leaf chemical properties in determining the response of leaf mass per area and photosynthesis of *Eucalyptus saligna* to industrial-age changes in $[CO_2]$ and temperature. *J Exp Bot*., 63, 5829-5841.

Yamauchi, D. and Mineyuki, Y. (2012) Demonstration of osmotically dependent promotion of aerenchyma formation at different levels in the primary roots of rice using a 'sandwich' method and X-ray computed tomography. *Ann Bot.,* **110**, 503-509.

Yin, X., Struik, P.C., Romero, P., Harbinson, J., Evers, J.B., Van Der Putten, P.E., Vos, J. (2009) Using combined measurements of gas exchange and chlorophyll fluorescence to estimate parameters of a biochemical C-3 photosynthesis model: a critical appraisal and a new integrated approach applied to leaves in a wheat (*Triticum aestivum*) canopy. *Plant Cell Environ.,* **32**, 448–464.

Yin, X. and Struik, P.C. (2009) Theoretical reconsiderations when estimating the mesophyll conductance to CO_2 diffusion in leaves of C_3 plants by analysis of combined gas exchange and chlorophyll fluorescence measurements. *Plant Cell Environ.,* **32**, 1513-1524 (with corrigendum in PC&E 33: 1595).

Table 1. Anatomical characteristics of leaves of two genotypes of tomato (mean ± 95% confidence interval[#], number n is pooled over three leaf samples)

Mesophyll type	Parameter	Genotype	
		'Doloresse'	'Growdena'
palisade	cell volume (μm^3) [s]	15760.3 ± 6288.6 (n=127)	39372.7 ± 11384.9 (n=73)
	sphericity (-)	0.755 ± 0.025 (n=127)	0.724 ± 0.033 (n=73)
	layer thickness (μm) [s]	56.3 ± 3.4 (n=9)	77.7 ± 6.1 (n=9)
	cell number density (mm^{-2}) [s]	1732 ± 299 (n=127)	1341 ± 73 (n=73)
	porosity (%) [°]	36 ± 9 (n=3)	29 ± 26 (n=3)
	exposed cell surface area to cell volume ratio (μm^{-1})*	0.18 ± 0.03 (n=127)	0.14 ± 0.11 (n=73)
	mesophyll cell area to leaf area ratio, S_m (*)	6.3 ± 1.4 (n=3)	7.4 ± 2.6 (n=3)
spongy	cell volume (μm^3)	4964.0 ± 3653.1 (n=335)	4923.9 ± 4767.5

		(n=383)
sphericity (-)	0.808 ± 0.077 (n=335)	0.837 ± 0.063 (n=383)
layer thickness (µm) [s]	68.1 ± 9.9 (n=9)	94.6 ± 9.4 (n=9)
cell number density (mm^{-2})	3848 ± 364 (n=335)	5105 ± 1042 (n=383)
porosity (%) °	60 ± 19 (n=3)	65 ± 11 (n=3)
exposed cell surface area to cell volume ratio (µm^{-1})*	0.25 ± 0.04 (n=335)	0.24 ± 0.12 (n=383)
mesophyll cell area to leaf area ratio, S_m *	6.7 ± 1.6 (n=3)	8.0 ± 0.9 (n=3)
total leaf porosity (%) [+]	41 ± 14 (n=3)	40 ± 6 (n=3)
stomatal density (mm^{-2}), abaxial side only	157.9 ± 87.5 (n=3)	133.5 ± 144.2 (n=3)

[#] 3 leaves from different plants per genotype, sample size 250 by 25à by 500 voxels, voxel size: 0.75 µm

° calculated based on the average layer thickness (h_i), surface area of the leaf sample (A) and total cell volume in the tissue (V_i):

$1 - V_i/(h_i A)$. These values exclude other tissues present in the sample, such as the epidermis and the vascular tissue.

* cell area only considers exposed area to the intercellular spaces

[+] calculated as the percentage of the number of voxels assigned as air space to total number of voxels of the leaf sample

[s] values are significantly different between genotypes at $p < 0.05$.
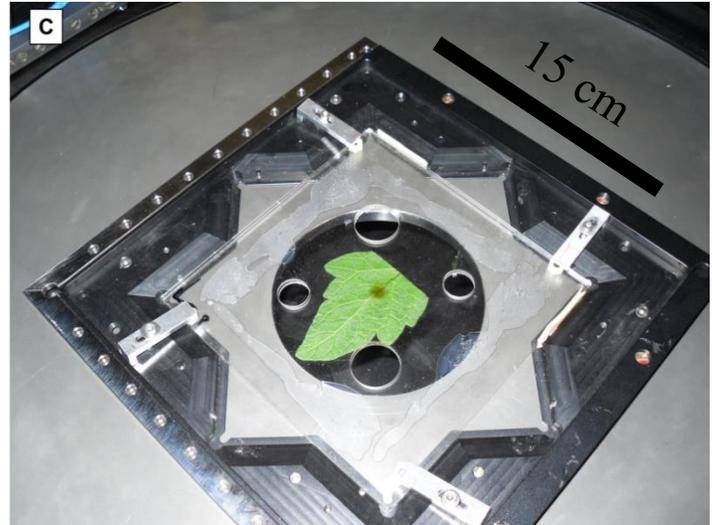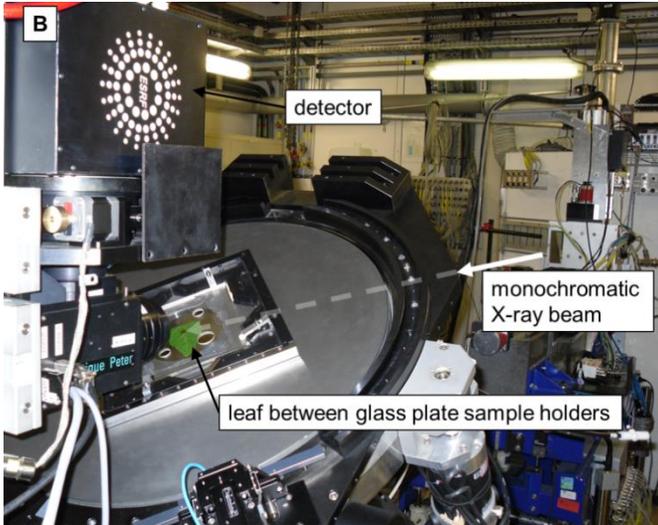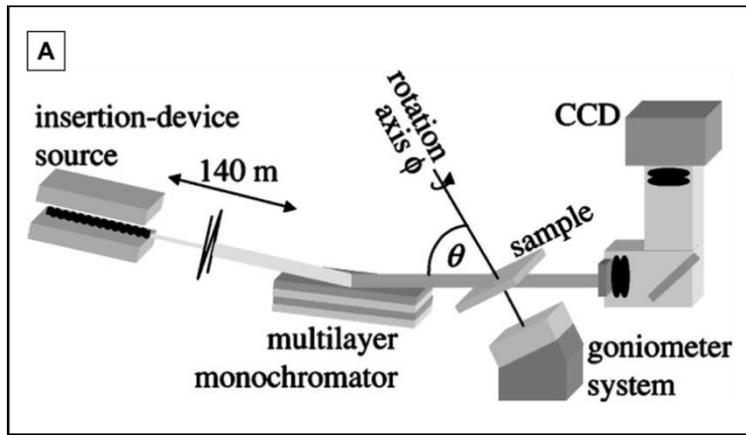
Figure 1. Principle of synchrotron X-ray laminography (Helfen et al. 2005). A. schematic lay-out of set-up. B. laminography set-up at beamline 19 of ESRF for imaging tomato leaves. C. sample holder with leaf.
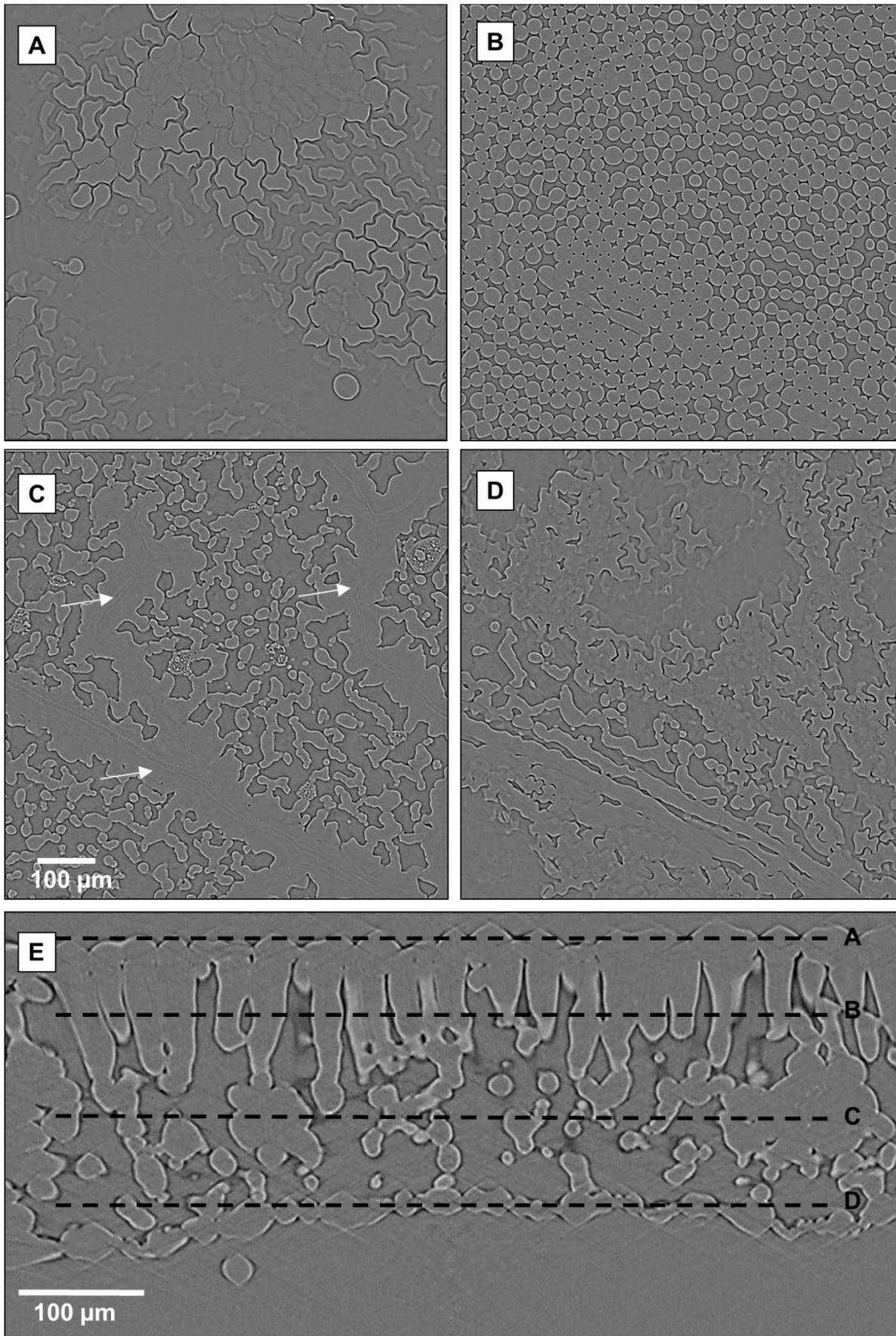
Figure 2. Synchrotron X-ray laminography cross sections of a 'Growdena' tomato leaf. A-D. horizontal cross sections through the leaf from adaxial epidermis (A), palisade parenchym (B), spongy parenchym and veins (arrows) (C) and abaxial epidermis (D). E. transverse cross section. Pixel size: 750 nm. Scale bar: 100 μm.
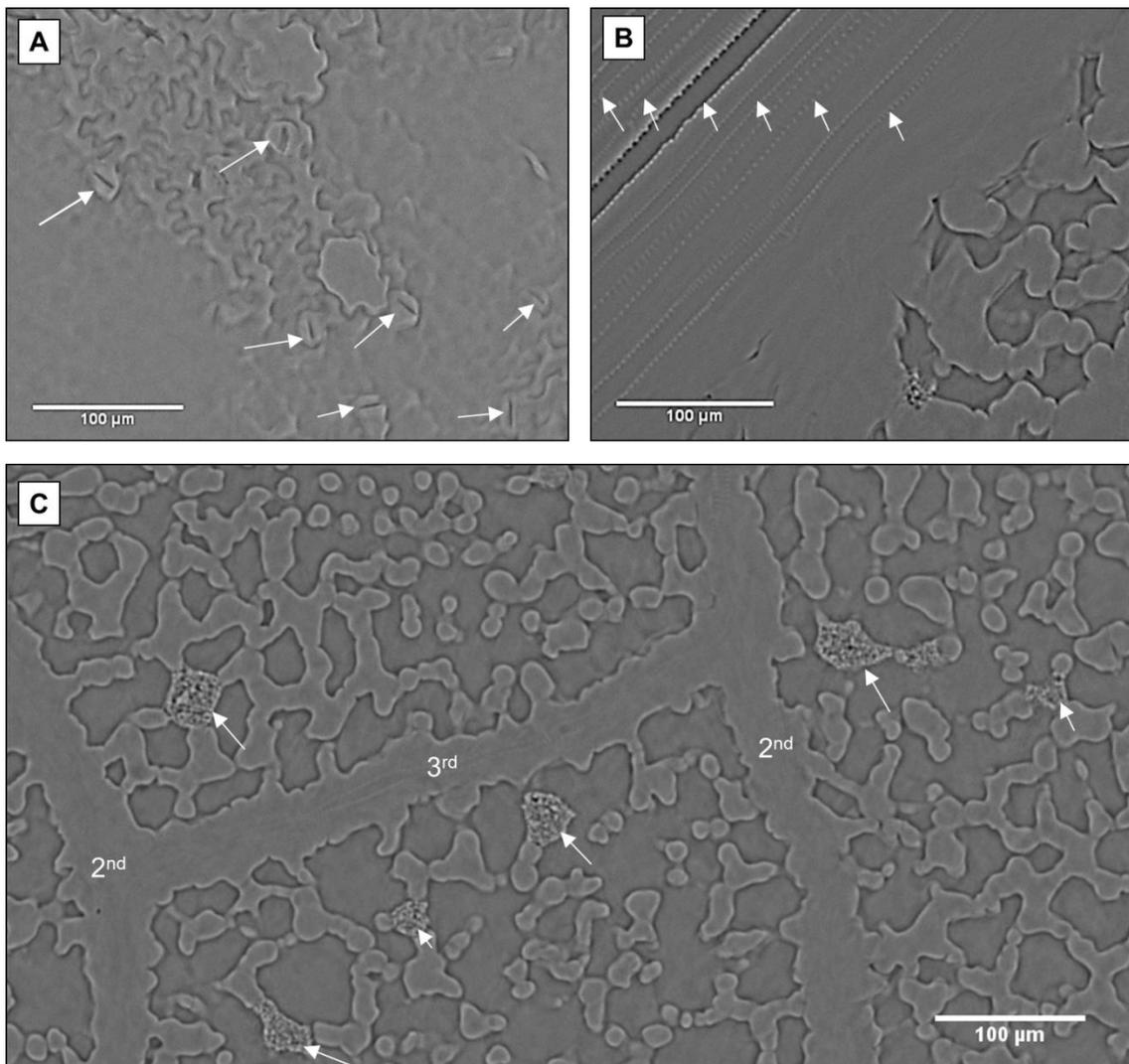
Figure 3. Microstructure features of tomato leaves visualised by synchrotron X-ray laminography. A. cross section through the abaxial epidermis of 'Doloresse' leaf. Stomata (arrows) can be identified by the shape of the bean shaped guard cells surrounding the stoma aperture seen as a straight line (closed stomata). B. cross section of a vascular bundle of the main vein of a 'Growdena' leaf. The trachedial structure of six different xylem vessels can be seen (arrows). One of the vessels is empty. The surrounding cells are packed very densely and thus individual cells cannot be well distinguished in the image. C. cross section through the veins and mesophyll of 'Growdena' leaf showing details of a cross-venulate venation structure of secondary (2nd) and tertiary (3rd) veins. From the veins, connections are made to the mesophyll cells. Arrows indicate cells with starch-containing plastids. Pixel size: 750 nm.
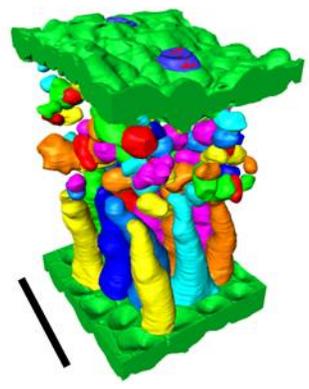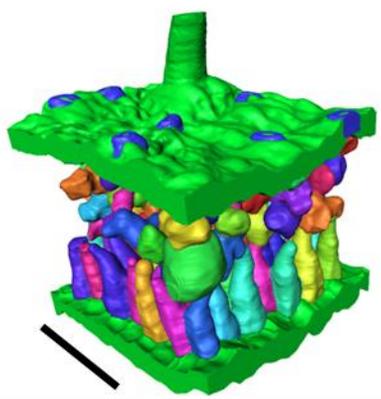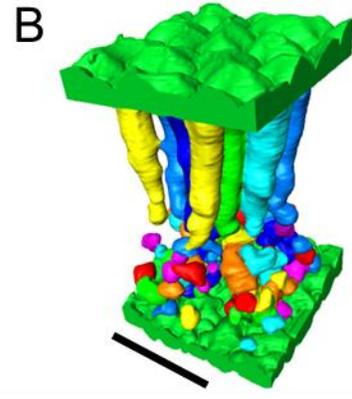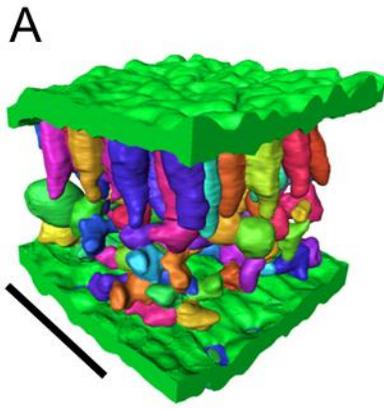
23
24
Figure 4. 3-D surface renderings of the segmented cellular structure of the mesophyll of 'Doloresse' (A) and
'Growdena' (B) tomato leaf samples with adaxial (top) and abaxial (bottom) views. Epidermis is colored in
green. Stomata in the abaxial epidermis are colored blue. Individual cells in the mesophyll are colored randomly
to render contrast. 3-D images are obtained from segmentation of samples (max. $250 \times 250 \times 500$ voxels) of
synchrotron X-ray laminographs at 750^3 nm^3 voxel size. Scale bars are 100 μm.
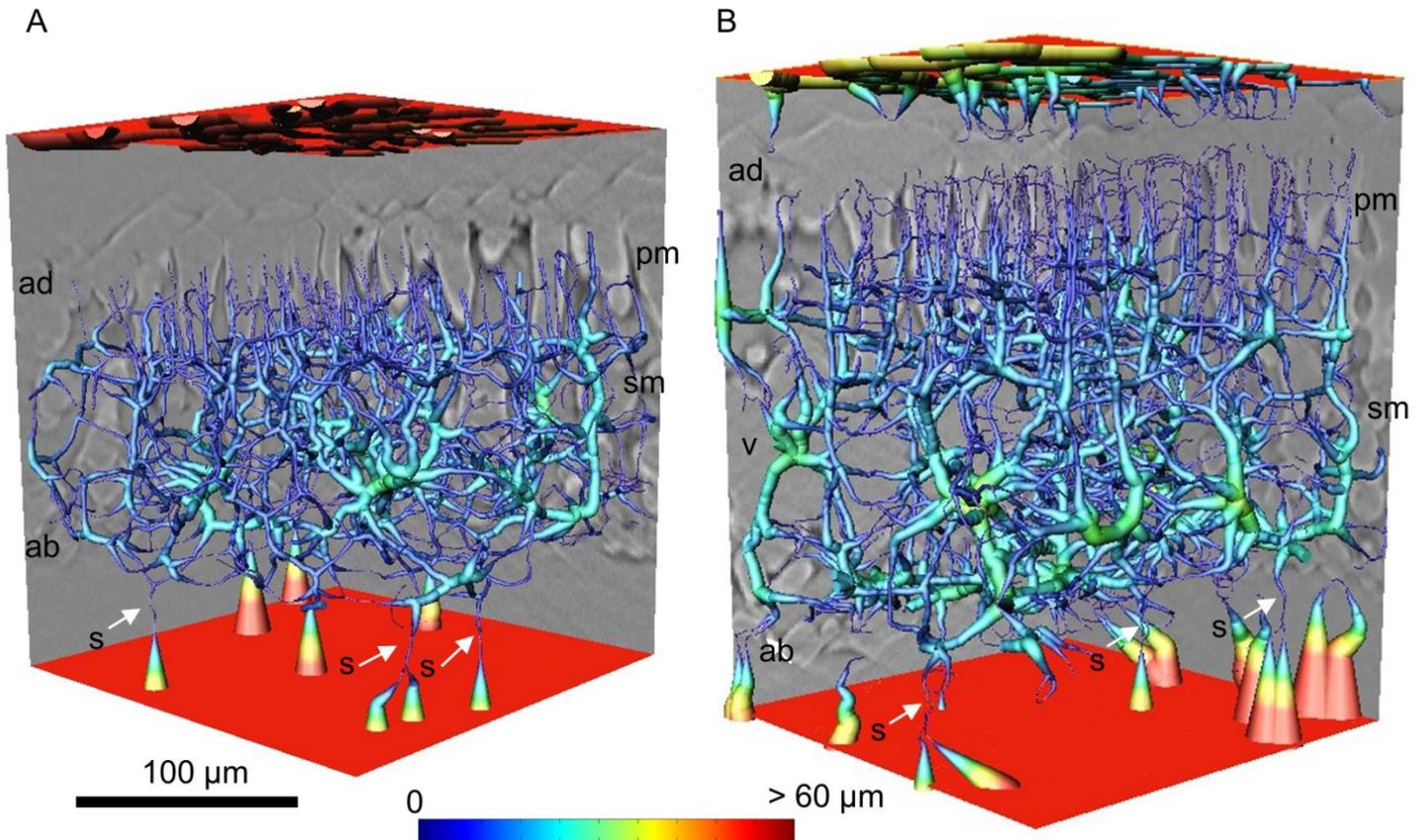
Figure 5. Pore space network analysis of tomato leaves of different genotypes: A. 'Doloresse', B. 'Growdena'. The red planes are the external air, that is connected to the internal airspace by means of the stomata (s), indicated by white arrows. The color of the network indicates the local radius of the pores inside the leaf tissue according to the given color scale: outside the leaf (top and bottom), the air space has infinite dimensions (red), the tiniest pore has a diameter of just over 1 µm. (ad: adaxial epidermis, ab: abaxial epidermis, s: stomata, pm: palisade mesophyll, sm: spongy mesophyll, v: vein). 3-D images are obtained from segmentation of samples (max. $250 \times 250 \times 500$ voxels) of synchrotron X-ray laminographs at 750^3 nm^3 voxel size.

39

40

41

42
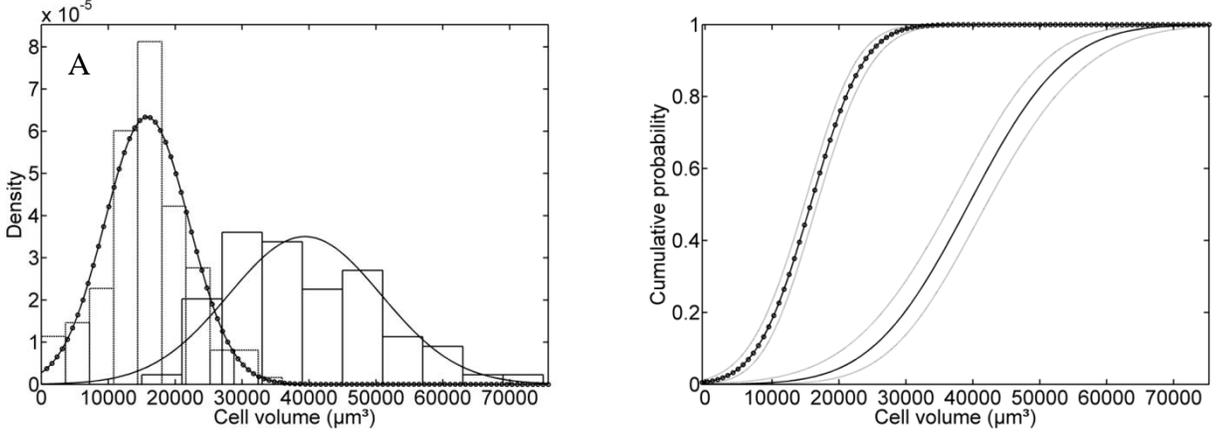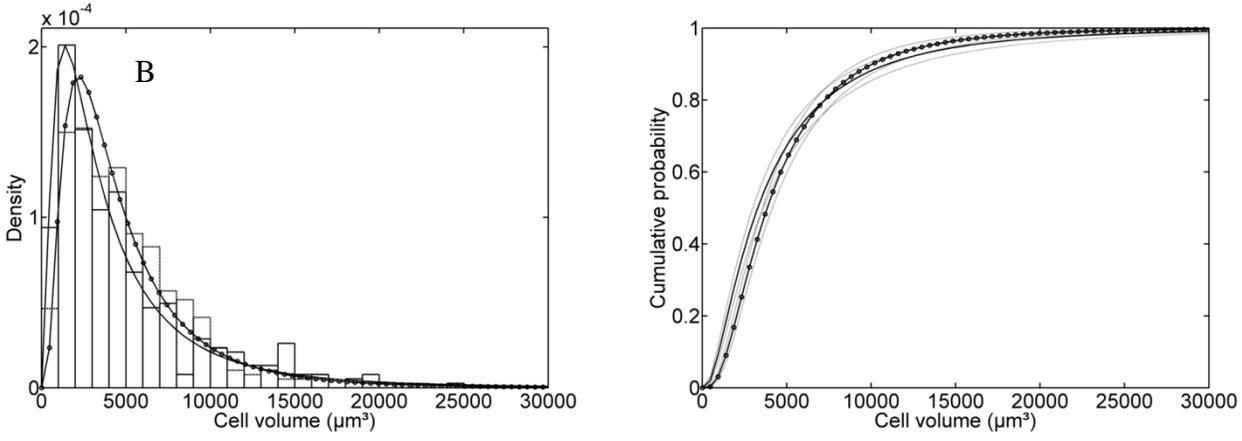
Figure 6. Cell volume probability density function (left) and cumulative probability (right) of palisade (A) and
spongy (B) mesophyll cells obtained from synchrotron X-ray laminography for 'Doloresse' (····) and
'Growdena' (——) tomato leaves. 95% confidence bounds are included on the cumulative distributions on the
right hand side figures. Data from three leaves from different plants per genotype, sample size 250 by 250 by
500 voxels, voxel size: 750^3 nm^3.

48
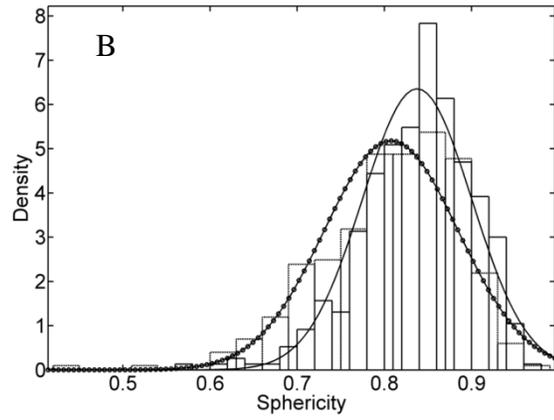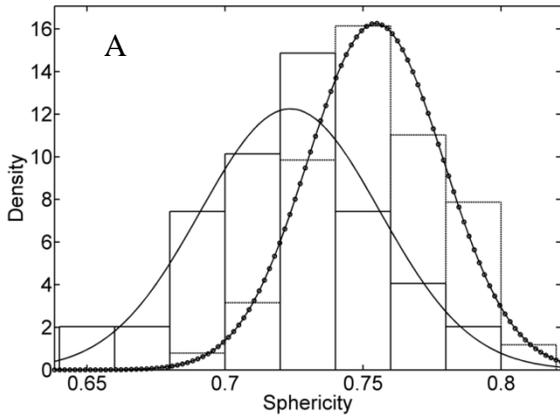
Figure 7. Cell sphericity probability density function of palisade (A) and spongy (B) mesophyll cells obtained from synchrotron X-ray laminography for 'Doloresse' (····) and 'Growdena' (—) tomato leaves. Data from three leaves from different plants per genotype, sample size 250 by 250 by 500 voxels, voxel size: 750^3 nm³.